



**HAL**  
open science

## **Influence of Sulfur and Water Vapor on High-Temperature Oxidation Resistance of an Alumina-Forming Austenitic Alloy**

Justine Allo, Samuel Jouen, Manuel Roussel, David Gibouin, Xavier Sauvage

► **To cite this version:**

Justine Allo, Samuel Jouen, Manuel Roussel, David Gibouin, Xavier Sauvage. Influence of Sulfur and Water Vapor on High-Temperature Oxidation Resistance of an Alumina-Forming Austenitic Alloy. *Oxidation of Metals*, 2021, 95 (5-6), pp.359-376. 10.1007/s11085-021-10028-9 . hal-03225463

**HAL Id: hal-03225463**

**<https://normandie-univ.hal.science/hal-03225463>**

Submitted on 17 Jun 2021

**HAL** is a multi-disciplinary open access archive for the deposit and dissemination of scientific research documents, whether they are published or not. The documents may come from teaching and research institutions in France or abroad, or from public or private research centers.

L'archive ouverte pluridisciplinaire **HAL**, est destinée au dépôt et à la diffusion de documents scientifiques de niveau recherche, publiés ou non, émanant des établissements d'enseignement et de recherche français ou étrangers, des laboratoires publics ou privés.

# Influence of Sulfur and Water Vapor on High-Temperature Oxidation Resistance of an Alumina-Forming Austenitic Alloy

Justine Allo<sup>1,2</sup>, Samuel Jouen<sup>1</sup>, Manuel Roussel<sup>2</sup>, David Gibouin<sup>1</sup>, Xavier Sauvage<sup>1</sup>

<sup>1</sup>Normandie Univ, UNIROUEN, INSA Rouen, CNRS, Groupe de Physique des Matériaux, 76000 Rouen, France

<sup>2</sup>Manoir Industries, 12 Rue des Ardennes – BP 8401 – Pîtres, 27108 Val de Reuil, France

Corresponding authors :

Justine Allo : [justine.allo@manoir.eu.com](mailto:justine.allo@manoir.eu.com)

Samuel Jouen : [samuel.jouen@univ-rouen.fr](mailto:samuel.jouen@univ-rouen.fr)

## ACKNOWLEDGEMENTS

This work was supported by the Agence National de la Recherche (ANR), project IPERS [grant number LAB COM – 15 LCV4 0003].

## ABSTRACT

The oxidation behavior of alumina-forming alloys was studied after oxidation treatments performed at 900°C for 24h in air or in steam. Alloys with sulfur contents ranging from 1 to 82 ppm in wt% were used. The influence of sulfur presence as a trace element as well as the presence of steam in the oxidizing atmosphere were investigated.

Under oxidation conditions, higher sulfur contents led to higher mass gains and the trend is more pronounced in steam than in air. Oxides were identified by Raman spectroscopy: a thin and continuous  $\alpha$ -Al<sub>2</sub>O<sub>3</sub> layer was formed at the metal-oxide interface in all cases. The mass gain differences were caused by other oxides formed at the surface of the samples – mainly spinel and Cr<sub>2</sub>O<sub>3</sub> – and in the internal oxidation zone too – mainly  $\alpha$ -Al<sub>2</sub>O<sub>3</sub> and  $\theta$ -Al<sub>2</sub>O<sub>3</sub> - indicating that the protectiveness of the alumina layer greatly depends on the sulfur content in the base material and the oxidizing atmosphere. In order to explain this phenomenon, oxide structures were analyzed at various scales using Scanning Electron Microscopy, Transmission Electron Microscopy and Nanoscale Secondary Ion Mass Spectrometry. Sulfur was detected at metal-oxide interfaces and also in the alumina layer in regions enriched with chromium. Besides, we demonstrate that steam oxidation leads to finer alumina grains as compared to air oxidation. Finally, the relationship between oxidation conditions, nanoscaled structural features and oxidation kinetics are discussed.

**KEYWORDS:** Sulfur traces; Steam; Alumina-forming alloys; High-temperature oxidation

Published in *Oxidation of Metals* (2021) 95:359–376

<https://doi.org/10.1007/s11085-021-10028-9>

## INTRODUCTION

Heat resistant alloys used in steam cracker furnaces are designed for creep resistance and high temperature corrosion resistance. Creep resistance is traditionally achieved by stabilizing an austenitic matrix (with 35-45 wt% of Ni) together with primary and secondary Cr-rich, Nb-rich and Ti-rich carbides (with 0.4-0.5 wt% of C). In the 1970's, HP grades containing 25 wt% of Cr and 35 wt% of Ni were traditionally used for cracking applications [1, 2]. The first evolution of this family has been Nb additions to improve creep resistance [3, 4], followed by Ti and few other micro-alloying strategies [4]. In order to increase the corrosion resistance, alloys with Cr contents up to 30-35 wt% were developed. The corrosion resistance of such alloys relies on the surface formation of a protective chromia layer. Nevertheless, oxide may volatilize and spall especially at temperature above 800°C in air-steam atmospheres typically used during decoking steps [5, 6]. Alumina-forming alloys are known to be stable at higher temperatures than chromia-forming alloys, especially under water vapor conditions [5 – 7]. A first patent has been published in 1981 for an alloy based on HP grade [8], but the development was stopped due to creep resistance problems [9]. Better understanding of creep mechanisms in Al-containing austenitic stainless alloys up to 1000-1050°C [10] has contributed to develop a new generation of alloys for steam cracking applications. It has been shown indeed that 3 to 5 wt% of aluminum could be successfully added leading to the formation of an Al<sub>2</sub>O<sub>3</sub> subscale. However, some impurities, like sulfur, are known to significantly affect alumina formation [5 – 7].

Besides, sulfur is known to have a substantial impact on the spalling resistance of alumina-forming alloys, especially during cyclic oxidation. Only a few ppm of sulfur increase mass losses during oxidation [11]. It has been shown that sulfur segregates at matrix / oxide interfaces at high temperatures [12 – 23], making such interface weaker [24, 25]. This effect has been attributed to a chemical modification of the interface. This sulfur segregation also promotes the growth of porosities at these interfaces [26].

A detrimental synergy between sulfur and oxidation under water vapor is often reported for the spalling resistance of alumina layers [14, 27 – 32]. It has been hypothesized that it could be due to segregated elements [14], such as hydrogen that would segregate at matrix / oxide interfaces like sulfur, further decreasing the oxide layer resilience [6].

More generally, sulfur influence on oxidation kinetics remains a controversial subject. Some authors have reported a significant increase of the oxide layer thickness and of its initial growth rate [33, 34], while others have shown only a decrease of the spalling resistance [5 – 7, 35].

Under water vapor conditions, the growth rate of metastable phases, like transition aluminas ( $\theta$  and  $\gamma$ ) or spinels, is higher in the transient stage [5, 6, 28, 32]. This phenomenon could have an impact on the  $\alpha$ -Al<sub>2</sub>O<sub>3</sub> growth as shown on FeCrAl [36, 37], on Fe-Al [5], and NiCrAl [27, 30, 31, 38] alloys. However, oxidation kinetics under water vapor are strongly dependent on the alloy composition, the atmosphere or the temperature and the mechanisms are not fully clarified yet.

In order to explain the combined effect of sulfur and water vapor influence on oxidation kinetics in alloys used in steam cracking applications, the oxidation behavior of an alumina-forming industrial alloy was studied both in air and in steam at 900°C. Alloys were specially cast with sulfur contents ranging from 1 to 82 ppm in wt%. The oxidized surfaces were characterized down to the nanoscale using Raman spectroscopy, NanoSIMS, SEM and TEM. A special emphasis was given on alumina nanoscaled layers, to identify crystalline defects and chemical modifications.

## MATERIAL AND METHODS

Dedicated alumina-forming austenitic alloys were centrifugally cast especially for this study. Their composition is based on the composition of Manaurite XAl4® shown in table 1, a commercial alloy of Manoir Industries for steam cracker applications. Six different sulfur contents have been considered: 1, 12, 24, 38, 48 and 82 wt ppm, measured by a nondispersive infrared spectrometer (ND-IR in a LECO analyzer). Tested alloys are named Al-X, with X= wt ppm of S.

**Table 1** Nominal compositions of the Manaurite XAl4 ® (in wt%)

Composition	C wt%	Al wt%	Ni wt%	Cr wt%	Ti wt%	Nb wt%	Fe wt%
<b>XAl4</b>	0.4 – 0.5	3.5 – 4.5	43 - 48	23 - 27	0 – 0.3	0 - 2	18 - 30

Figure 1 shows the typical as cast microstructures formed in alloys Al-1 and Al-82. Large grains of austenitic matrix (grey contrast) are dendrites grown during solidification. They are surrounded by two kinds of carbides: Cr-rich  $M_7C_3$  (darkly imaged) and (Nb,Ti)-rich MC (brightly imaged). More information on microstructures and phase identification in such alloys can be found in [10, 39, 40].

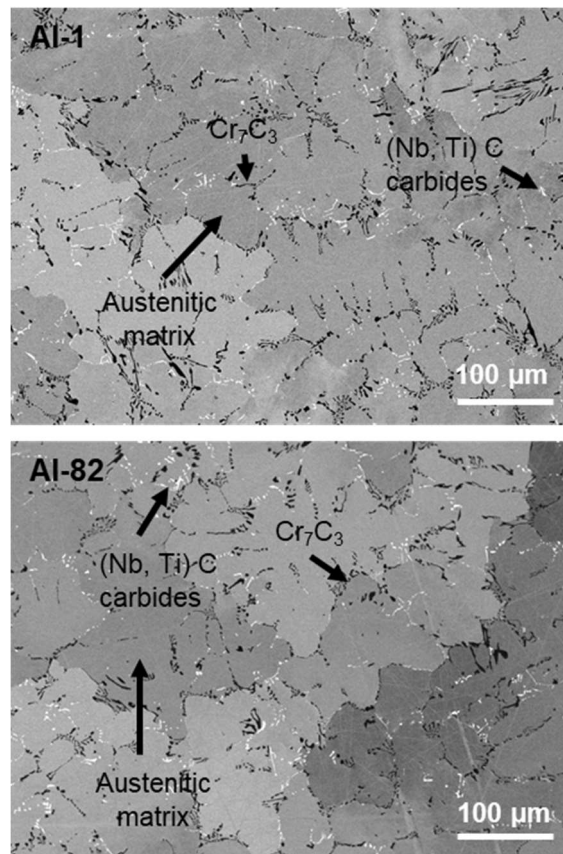


**Fig. 1** Typical as cast microstructures of Manaurite XAl4 (Al-1 and Al-82 samples, SEM images)

10 X 15 X 2 mm<sup>3</sup> coupons were machined out of the 6 alloys in order to perform oxidation tests. Prior to the oxidation tests, surfaces were prepared by grit polishing using SiC paper down to 800 grit, and samples were cleaned in an acetone ultrasonic bath. Mass measurements were carried out before and after oxidation with three samples of each alloy using a balance with a reliability of 0.1 mg.

Oxidation tests were performed for 24h at 900°C in a tubular furnace in laboratory air and in a mixture of 2/5 Ar-3/5 H<sub>2</sub>O by volume including some N<sub>2</sub> impurities. Samples were introduced in a cold furnace and heated up at a

rate of 900°C/h followed by the isothermal oxidation treatment. Samples were cooled down slowly (180°C/h) in the furnace to limit spalling.

In order to identify crystal structures of the main phases formed during oxidation tests, Raman spectroscopy was performed with a Horiba Jobin-Yvon LabRam Aramis Raman spectrometer, equipped with two lasers of wavelength 632.8 nm and 532 nm. The laser beam was focused on the sample using a 100X objective giving a spot size smaller than 1 µm.

Prior to cross-sectional SEM investigations, samples were first coated with a thin gold layer (100-200nm) in a vacuum metallizer and then a thicker electrolytic copper layer (about 20 µm) was deposited for an optimal protection of oxidized surfaces. These samples were then embedded in a conductive resin and mechanically polished with ¼ µm diamond paste for the final step.

SEM observations were carried out with a ZEISS LEO 1530 XB operating at 15kV, with images recorded using a secondary electron detector.

Transmission electron microscopy (TEM) samples were prepared using a FEI Helios dual-beam SEM-focused ion beam, using Xe ions. Samples were protected through the application of an in situ deposited platinum layer; then trenches were dug and a lamella was extracted using a micromanipulator. Samples were then thinned to electron transparency at 30kV and 12kV.

TEM observations were carried out with a probe corrected JEOL ARM-200F operated at 200kV. Elemental mapping was carried out using Energy Dispersive X-ray Spectroscopy (EDX) with an Oxford Instruments X-max detector (collection angle 0.7 sr). Grain size quantification was done from scanning transmission electron microscopy (STEM) images on at least 30 different grains on each samples.

High-resolution nanoSIMS analyses were carried out using a CAMECA NanoSIMS 50 with a 16keV Cs<sup>+</sup> primary beam. <sup>52</sup>Cr<sup>16</sup>O<sup>-</sup>, <sup>27</sup>Al<sup>16</sup>O<sup>-</sup>, and <sup>32</sup>S<sup>-</sup> ions were simultaneously collected for mapping.

## RESULTS

The mass gain (relative to sample surfaces) of samples oxidized in air and steam is plotted as a function of sulfur content in figure 2. From 1 to 38 wt ppm of sulfur, mass changes under both atmospheres are extremely small and remain near the detection limit (about  $0.1 \pm 0.1$  mg/cm<sup>2</sup>). At sulfur contents higher than 40 wt ppm, mass variations are more significant and a strong correlation with sulfur level is exhibited. For the Al-82 the mass gain in air (up to  $0.2 \pm 0.1$  mg/cm<sup>2</sup>) is indeed twice larger than for Al-1 and it raises up to  $0.54 \pm 0.1$  mg/cm<sup>2</sup> in steam. This data indicates that there is a strong combined effect of the sulfur content and of the oxidation atmosphere.

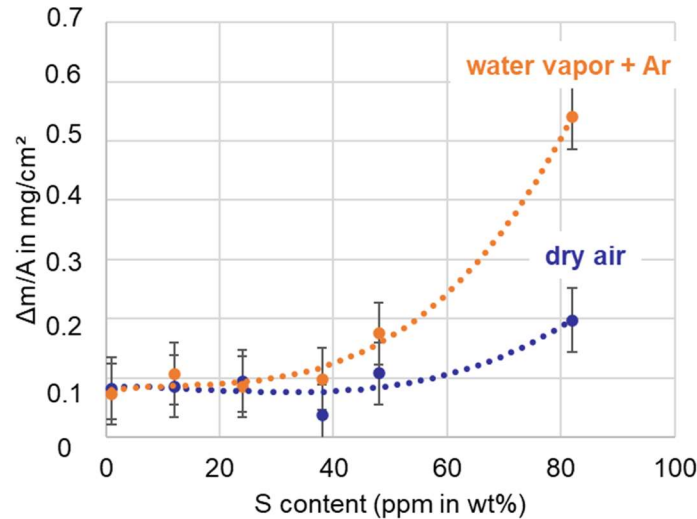


**Fig. 2** Influence of sulfur on the mass variations of samples oxidized at 900°C during 24h under dry air and water vapor + Ar mixture

Three representative alloys oxidized in both atmospheres were selected for further analysis: a low sulfur content (Al-1), an intermediate case (Al-48) and a high sulfur content (Al-82).

Figure 3 shows the cross-sectional samples of Al-1, Al-48 and Al-82 after 24h isothermal oxidation at 900°C in dry air and in water vapor. On the top surface, the thick electrolytic Cu and thin gold protective layers are clearly exhibited. Below these layers, two kinds of features appear: thin oxide layers (zone A circled on figure 3.c), and protuberated oxides (zone B circled on figure 3.f) always combined with internal oxidation (zone C circled on figure 3.f).

The identification of phases located in these different zones was performed using Raman spectroscopy on cross-sectional samples. Figure 4 shows representative Raman spectra recorded respectively on zones A, B and C. In zone A, two phases could be clearly identified. Raman shifts located at 302 cm<sup>-1</sup>, 348 cm<sup>-1</sup> and 555 cm<sup>-1</sup> are attributed to Cr<sub>2</sub>O<sub>3</sub> [41], and those at 401 cm<sup>-1</sup>, 656 cm<sup>-1</sup> and 694 cm<sup>-1</sup> to spinel structure [42]. In the spinel structures, the position of the highest wavenumber Raman peak, which is also the most intense, has a great dependence on the nature of the cation in the octahedral sites. In the present case, the strong and broad peak at 694 cm<sup>-1</sup> is consistent with the presence of mainly Cr<sup>3+</sup> cations in the octahedrally coordinated sites. Unfortunately, others Raman peaks related to this phase are not strong enough to determine the exact stoichiometry of the oxide [42, 43]. The alloys of the present study contain a significant amount of Al. Thus, aluminium oxide is expected to form. However, probably because of a low volume fraction and overlaps with other oxides, Raman modes of alumina phases cannot be unambiguously identified. Some authors have shown however that polymorphs of alumina could be identified when they contain Cr<sup>3+</sup> impurities, thanks to the photo-induced fluorescence peaks of Cr<sup>3+</sup> ions occurring in the Raman shift range [1000-1800] cm<sup>-1</sup>. Thus Raman spectra were recorded in zone A using a He-Ne laser (figure 4.b) and they show indeed two well-defined peaks at 1370 cm<sup>-1</sup> and 1400 cm<sup>-1</sup> which are characteristic of Cr<sup>3+</sup> fluorescence in α-Al<sub>2</sub>O<sub>3</sub> [44 – 46], proving also the presence of this later phase in the oxide scale.

Similar oxides were detected in zone B (protuberated oxides), but interestingly the main Raman mode of  $\text{Cr}_2\text{O}_3$  (at  $551\text{ cm}^{-1}$ ) was often much more intense than the main spinel' peak, suggesting a larger volume fraction of  $\text{Cr}_2\text{O}_3$  in this thick external oxide layer as compared to the thinner of zone A (figure 4.a). Besides, in zone C (internal oxidation area), two different polymorphs of alumina were identified with a pair of fluorescence peaks located at  $1179\text{ cm}^{-1}$  and  $1239\text{ cm}^{-1}$  and another at  $1374\text{ cm}^{-1}$  and  $1404\text{ cm}^{-1}$  that could be attributed respectively to  $\theta\text{-Al}_2\text{O}_3$  [45, 46], and  $\alpha\text{-Al}_2\text{O}_3$ . AlN is also detected locally with Raman peaks located at  $617\text{ cm}^{-1}$  and  $657\text{ cm}^{-1}$ [47], on platelet-like morphologies, shown on figures 3.d, 3.e and 3.f.

In summary, thin oxide layers (zone A) are composed of a spinel phase,  $\text{Cr}_2\text{O}_3$  and  $\alpha\text{-Al}_2\text{O}_3$ . Thick oxide layers (zone B) contain mainly  $\text{Cr}_2\text{O}_3$ , with a small amount of spinel and  $\alpha\text{-Al}_2\text{O}_3$  too. Last, the internal oxidation zone located under zone B (zone C) contains AlN and two alumina phases,  $\alpha\text{-Al}_2\text{O}_3$  and  $\theta\text{-Al}_2\text{O}_3$ .

A more precise localization of the different compounds identified by Raman spectroscopy was established based on SEM image contrasts (figures 3). For the lowest sulfur content (figures 3.a and 3.b), after oxidation in air and steam, the oxide structured layer is typical of zone A : the alloy matrix is covered by a thin layer of  $\alpha\text{-Al}_2\text{O}_3$ , then  $\text{Cr}_2\text{O}_3$  and spinel on the top. At medium sulfur content (figures 3.c and 3.d), some protuberated oxides with internal oxidation (such as zone B and C) were also formed locally, and this phenomenon is more pronounced after oxidation under vapor conditions. At the highest sulfur content (figures 3.e and 3.f), the growth of protuberated oxides with underneath internal oxidation is generalized and more especially under water vapor. On protuberated oxides (zone B), non oxidized matrix grains were also observed in the chromia layer above the alumina layer. Thus, it turns out that the structure, the thickness and the morphology of oxidation affected layers strongly depend both on the sulfur content and the oxidation atmosphere. Both highest sulfur levels and water vapor conditions

give rise to more numerous protuberated oxides with underneath internal oxidation zones. These observations are fully consistent with mass variation evolutions displayed on figure 2.

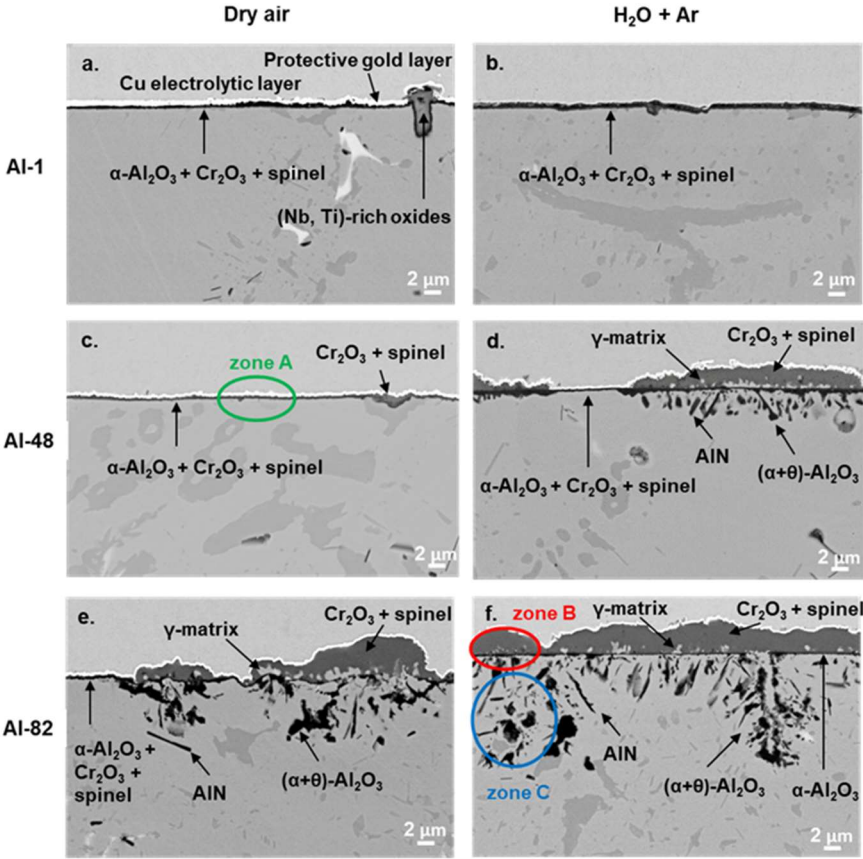


**Fig. 3** Cross-sectional SEM observations of Al-1 (a, b), Al-48 (c, d) and Al-82 (e, f) oxidized 24h at 900°C under dry air (a, c, e) and under water vapor mixture(b, d, f)

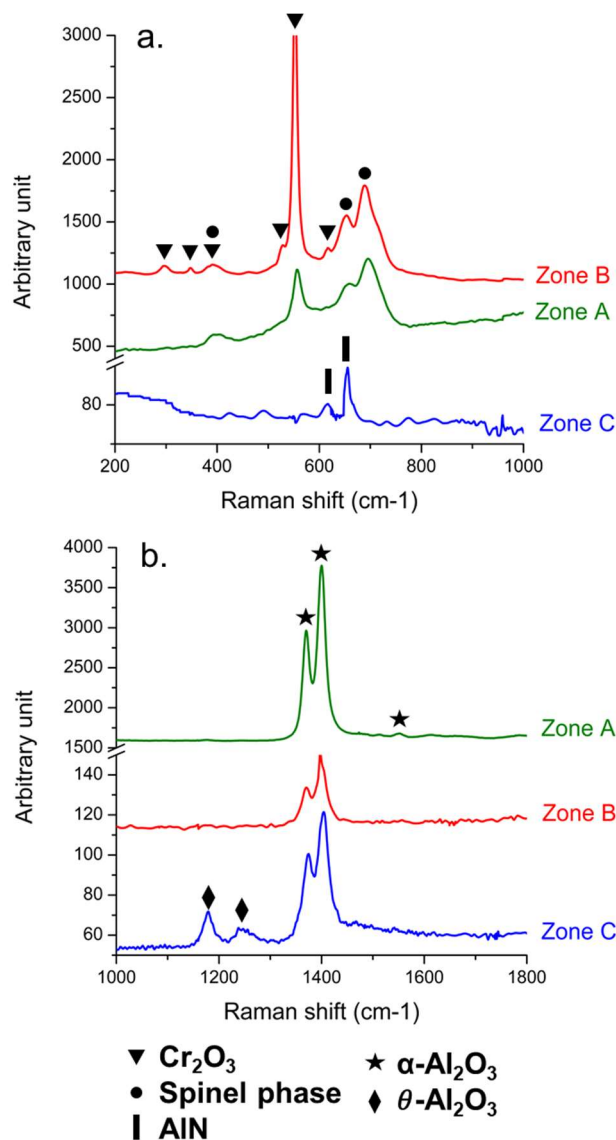


**Fig. 4** Raman spectra collected in zones A, B and C indicated on Fig. 3. Spectra recorded in the low-wavenumbers range [200 to 1000] cm<sup>-1</sup> were obtained using a 532 nm radiation and laser power of ~13 mW (a) In the high-wavenumbers range [1000 to 1800] cm<sup>-1</sup>, spectra were recorded with a 632.8 nm radiation and laser power of 0.2 mW was used (b)

A thin  $\alpha$ -alumina layer was formed on the surface of samples, in thin oxide layers and in protuberated oxides zones. However, the  $\alpha$ -alumina layer formed in zones B is apparently less protective. Indeed, these zones contained a thick spinel + Cr<sub>2</sub>O<sub>3</sub> layer with matrix grains which were not oxidized, and ( $\alpha$  +  $\theta$ )-Al<sub>2</sub>O<sub>3</sub> internal oxidation, with some AlN particles.

In order to explain this phenomenon, structures and compositions of alumina layers were analyzed by transmission electron microscopy. Nanoscale secondary ion mass spectrometry was also used for sulfur localization.

A typical image of the structure of the oxide layer in zone A is shown on figure 5. On the cross-sectional STEM image recorded with a high angle annular dark field (HAADF) detector (figure 5.a), the different oxides are revealed with a Z contrast. Additional information about the distribution of alloying elements was collected thanks to EDX mapping (figures 5.b, c, d, e and f). Phase identification was also carried out using electron diffraction, however due to the nanoscaled structure of oxide layers and the large number of possible oxide diffraction spot overlaps, it has not been possible to collect reliable and quantitative information, therefore these data are not shown here.

The matrix is located at the bottom, it contains a high Cr, Fe and Ni concentration and a low O level. The Cr rich zone on the right hand side is attributed to a chromium-rich  $M_7C_3$  carbide. Three different layers with a high amount of O are stacked above the matrix. The top layer contains mainly Cr, Fe, Ni, Al and O which is consistent with the spinel phase. Below, a thin layer with a high amount of Cr and O is exhibited, consistent with the  $Cr_2O_3$  phase. In contact with the austenitic matrix, the last layer is exclusively enriched in Al and O, corresponding to the  $\alpha-Al_2O_3$  phase.

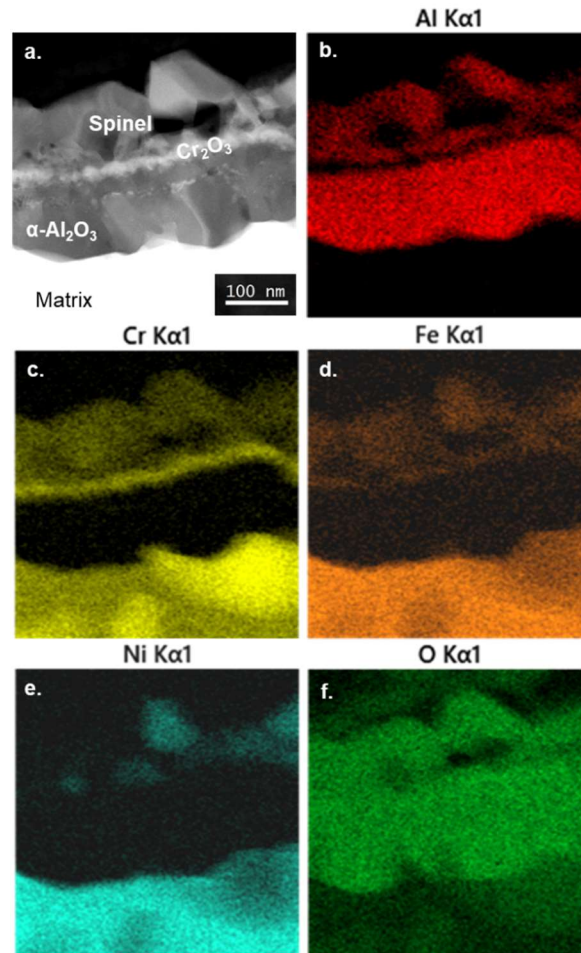


**Fig. 5** Cross-sectional STEM-HAADF image (a) and EDX elemental maps of Al (b), Cr (c), Fe (d), Ni (e) and O (f) ( $K\alpha$  rays) of Al-1 oxidized 24h at 900°C under dry air

The mean thickness and the grain size of  $Al_2O_3$  layers have been estimated from STEM images in regions corresponding to zone A (thinnest oxide layers) of Al-1 and Al-82 alloys oxidized under both atmospheres. In the  $Al_2O_3$  layer, grains exhibit a columnar structure, thus, two parameters have been chosen, namely the layer thickness and the apparent grain width, as depicted on figures 6.a and 6.b. The thickness is similar for both samples, with a thickness of about 90 nm whatever the oxidation conditions (figure 6.c). Meanwhile, the grain width appears relatively similar for both alloys but strongly depends on the oxidation atmosphere. Indeed, after oxidation under dry air, alumina grain width is  $90 \pm 19$  and  $84 \pm 12$  nm for Al-1 and Al-82 alloys respectively, while after oxidation under water vapor, alumina grain width is  $57 \pm 13$  and  $52 \pm 4$  nm for Al-1 and Al-82 alloys respectively (figure 6.d). Thus, the oxidation atmosphere seems to significantly affect the nucleation and growth mechanisms of alumina grains.

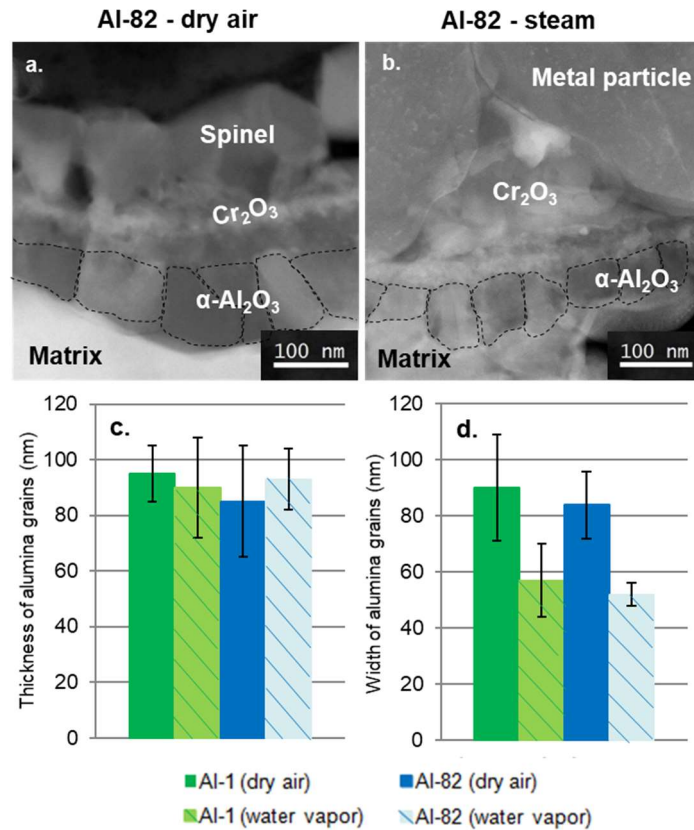


**Fig. 6** STEM-HAADF images of Al-82 oxidized under dry air (a) and under water vapor (b) showing alumina grain size, measured thickness (c) and width (d) of alumina grains in samples Al-1 and Al-82 oxidized 24h at 900°C under dry air and under water vapor

Since mass gain measurements and SEM observations revealed also a strong combined effect of the sulfur content and of the oxidation atmosphere, further analyses were carried out to localize the sulfur within the complex multilayer oxide structure.

The NanoSIMS technique is known to be particularly sensitive to light elements and is well adapted to the localization of sulfur traces [48, 49]. NanoSIMS elemental maps of <sup>52</sup>Cr<sup>16</sup>O<sup>-</sup>, <sup>27</sup>Al<sup>16</sup>O<sup>-</sup> and <sup>32</sup>S<sup>-</sup> ions collected in a cross sectional sample of the Al-82 alloy oxidized under water vapor are displayed on figure 7.a. The few micrometers thick internal oxidation zone is clearly exhibited with Al rich particles, corresponding most probably to α and θ alumina phases. On the top right corner, a 3 μm Cr rich layer corresponding to the Cr<sub>2</sub>O<sub>3</sub> layer appears. Inside this layer, zones with low signals correspond most probably to non oxidized metallic particles. Last, the thin continuous Al<sub>2</sub>O<sub>3</sub> layer located between Cr<sub>2</sub>O<sub>3</sub> and the matrix is highlighted by the strong <sup>27</sup>Al<sup>16</sup>O<sup>-</sup> ion signal. <sup>32</sup>S<sup>-</sup> enrichments are exhibited in the continuous α alumina layer, around metallic particles inside the chromia layer and at interfaces between internally nucleated Al<sub>2</sub>O<sub>3</sub> particles and the austenitic matrix. Figure 7.b shows a NanoSIMS elemental map combining <sup>52</sup>Cr<sup>16</sup>O<sup>-</sup>, <sup>27</sup>Al<sup>16</sup>O<sup>-</sup> and <sup>32</sup>S<sup>-</sup> signals obtained in the cross section of the Al-82 alloy oxidized under dry air. The thin oxide layer that is exhibited is typical of zone A (figure 3). <sup>32</sup>S<sup>-</sup> enrichments are observed in the oxide scale but this layer is too thin to obtain a relevant contrast on elemental maps. So for a better localization of these different signals, a linear profile was computed from this map (figure 8) starting in the austenitic matrix at the bottom, up to the spinel layer.

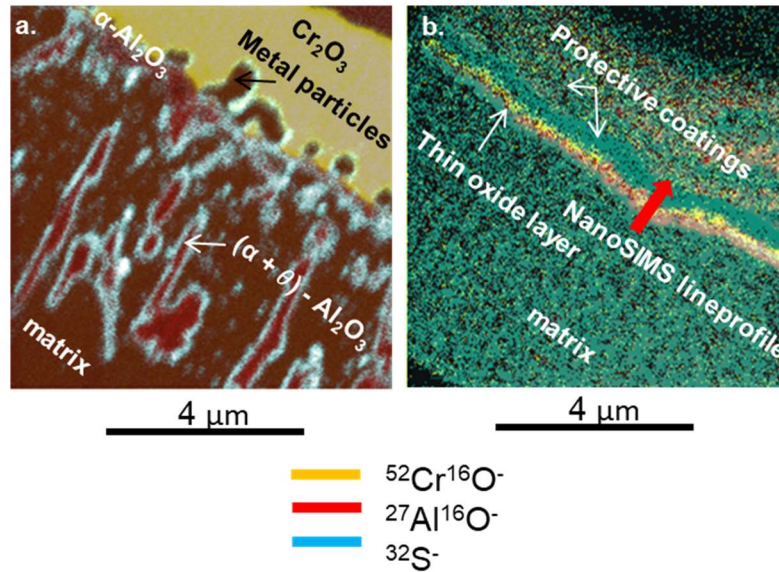


**Fig. 7** Superposition of NanoSIMS elemental maps of  $^{52}\text{Cr}^{16}\text{O}^-$ ,  $^{27}\text{Al}^{16}\text{O}^-$  and  $^{32}\text{S}^-$  ions collected in Al-82 oxidized for 24h at  $900^\circ\text{C}$  under water vapor (7.a) and under dry air (7.b)

The signal of  $^{52}\text{Cr}^{16}\text{O}^-$  exhibits two maxima, corresponding to  $\text{Cr}_2\text{O}_3$  and spinel phases. A large zone, with a thickness ranging from  $0.35$  to  $0.75\ \mu\text{m}$ , exhibits a strong  $^{27}\text{Al}^{16}\text{O}^-$  signal. According to figure 5, the spinel phase located on the top contains some Al and the  $\text{Cr}_2\text{O}_3$  layer below is very thin. Thus this Al rich zone should contain almost the entire oxide layer. A maximum of the  $^{32}\text{S}^-$  signal clearly appears between the matrix and the  $\alpha$ -alumina layer, however because of the limited spatial resolution (about  $50\ \text{nm}$ ), it is not possible to conclude about the exact location of sulfur within the complex nanoscale structure of the oxide layers revealed by NanoSIMS.

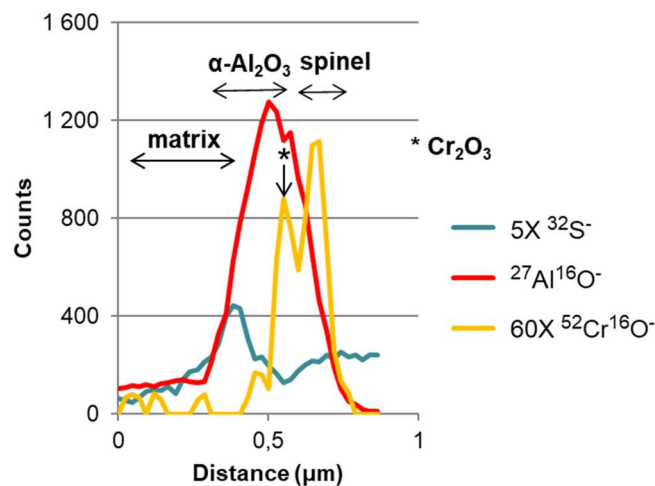


**Fig. 8** Line profiles of  $^{52}\text{Cr}^{16}\text{O}^-$ ,  $^{27}\text{Al}^{16}\text{O}^-$  and  $^{32}\text{S}^-$  extracted from map (Fig.7.b) through the oxide layer along the direction indicated by the red arrow

To collect more detailed information about the exact location of sulfur, some STEM-EDX line profiles were collected on the Al-82 alloy oxidized under water vapor (figure 9). The EDX line profile recorded inside the external alumina layer (figure 9.b), shows as expected, a strong oxygen and aluminum enrichment, but also periodic spatial fluctuations of the chromium concentration with a typical length scale of about  $100\ \text{nm}$ . The sulfur content is very low (local maximum up to  $1\ \text{at}\%$ ) but it is obviously correlated with local Cr enrichment.

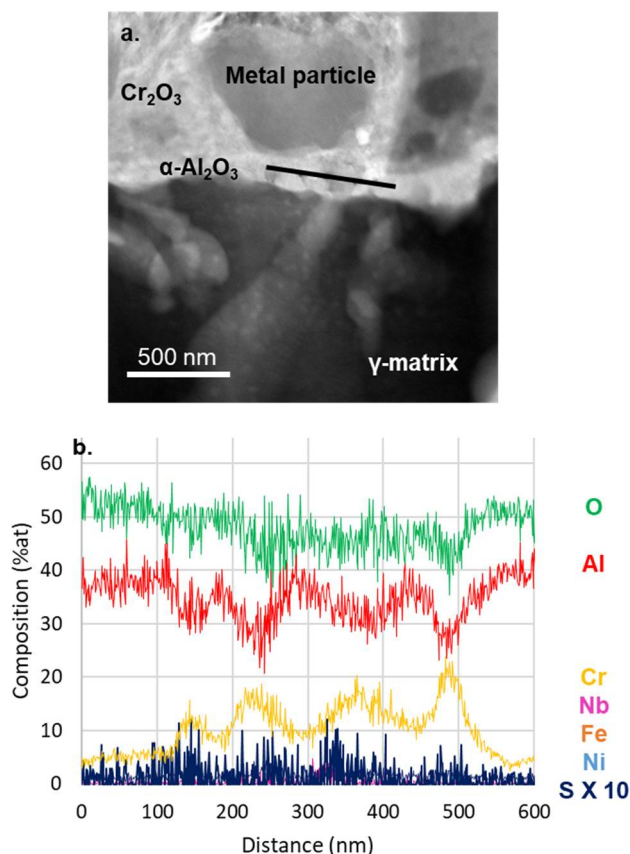


**Fig. 9** Al-82 oxidized under water vapor mixture, (a) cross-sectional STEM image; (b) EDX line profile inside the external alumina layer along the black line indicated on (a)

In summary, after oxidation under dry air and under water vapor at 900°C of Al-82, sulfur is located at all alumina interfaces, in internal and external oxides. Sulfur is also found in the alumina layer, in chromium rich zones, periodically distributed inside the  $\alpha\text{-Al}_2\text{O}_3$  layer. Last some sulfur was also detected around metal particles in protuberated oxides (zone B). It is important to note that similar investigations were carried out in the alumina layer formed on the Al-1 alloy oxidized under both atmospheres. As expected, sulfur was never detected (data not shown here) and chromium concentration fluctuations inside the  $\text{Al}_2\text{O}_3$  layer were not found neither.

## DISCUSSION

Sulfur presence in alumina-forming alloys is known to have a negative impact on spalling resistance [12 – 19, 21 – 23, 25]. In this study, no spalling of oxide scale was observed. This is most probably the result of the specific oxidation treatment conducted in the present study (isothermal oxidation and slow cooling of the samples in the furnace).

Mass gain measurements (Fig. 2) demonstrated two very important features for the considered alumina forming austenitic alloy: i) higher sulfur contents lead to faster oxidation kinetics; ii) at sulfur concentrations above 40ppm, the oxidation kinetics is significantly accelerated under water vapor conditions.

To understand the underlying mechanisms, oxidized surfaces have been investigated to identify the different phases and the related microstructures. Similar oxides have always been detected from the top surface to the core material, namely spinel phases,  $\text{Cr}_2\text{O}_3$  and  $\text{Al}_2\text{O}_3$ . This sequence is fully consistent with the respective formation enthalpies of these three oxides [5, 6]. On a microstructural point of view, large differences have however been revealed. SEM data (Fig. 3) revealed that slow oxidation kinetics are always connected with a thin (less than a micrometer in the tested conditions), continuous and regular multilayer oxide structure. While faster oxidation rates (at medium sulfur content under water vapor or for high sulfur content in air or water vapor conditions) are connected to the growth of thick (few microns) protuberated oxides made of spinel and  $\text{Cr}_2\text{O}_3$  standing over a thin continuous  $\text{Al}_2\text{O}_3$  layer and a relatively thick region (up to 10 micrometers) exhibiting internal oxidation and

nitridation of Al. Thus, it seems that under the tougher conditions (high sulfur and water vapor), the continuous  $\text{Al}_2\text{O}_3$  layer is not protective anymore, allowing faster downward diffusion of  $\text{O}^{2-}$  and upward diffusion of  $\text{Cr}^{3+}$ .

The continuous nanoscaled  $\text{Al}_2\text{O}_3$  layers for all alloys and all conditions exhibit the same  $\alpha$ -alumina phase and similar thicknesses (about  $90\pm 10\text{nm}$ , Fig. 6). A significant microstructural difference was found however between samples oxidized in air and in water vapor conditions: columnar alumina grains are almost half the thickness under water vapor than under dry air (55 against  $90\pm 10\text{nm}$  respectively, Fig. 6). Water vapor is known to affect the oxidation mechanisms of alumina forming alloys leading usually to more transient oxides [5, 6, 27, 28, 32, 36 – 38]. More generally, Gulbransen and Copan [50] demonstrated also in experiments carried out with pure Fe at  $450^\circ\text{C}$  that water vapor facilitates oxide nucleation by promoting surface diffusion. Thus, in the present case, more metastable  $\text{Al}_2\text{O}_3$  nucleation sites probably appeared in the early stage, leading to a larger number density of growing alumina grains with thinner lateral dimensions.

Since the mobility of  $\text{O}^{2-}$  and  $\text{Al}^{3+}$  in  $\alpha$ -alumina is dominated by grain boundaries diffusion [51 – 54], then it could be expected that thinner alumina grains would create a weaker barrier and then give rise to faster oxidation kinetics in long term exposures. A pre-oxidation treatment under dry air before utilization under steam conditions would probably be beneficial even when the sulfur is below 30 ppm. However, after only 24h oxidation at  $900^\circ\text{C}$ , our experiments carried out on the Al-1 alloy show that the smaller alumina grains that have nucleated under water vapor (Fig.6) do not give rise to any other detectable microstructural differences as compared to air oxidation (Fig.3). This clearly demonstrates that sulfur plays a predominant role and that water vapor simply acts as an accelerating agent in the case of high S alloys.

Thanks to NanoSIMS (Figs. 7, 8) and STEM-EDS (Fig. 9), sulfur was localized in various location of the complex oxide surface microstructure: i) at interfaces between internally nucleated  $\text{Al}_2\text{O}_3$  particles and the austenitic matrix and around metallic particles located inside the chromia layer, both corresponding to grain boundaries where sulfur segregation is well known [55 – 57]; ii) inside the nanoscaled continuous  $\alpha$  alumina layer. In this layer, TEM-EDS data revealed also significant fluctuations of the S concentration spatially correlated to Cr concentration fluctuations. The co-segregation of sulfur and chromium in metallic alloys has already been experimentally observed [33, 58, 59] Chromium-sulphur compounds can be expected, or some authors have hypothesized that it could result from the formation of nanoscaled chromium sulfides at the interface between the matrix and the oxide layer in FeCrAl alloys [60, 33]. Similar mechanisms could occur in the alloy of the present study where chromium sulfides could nucleate inside the alumina layer. Considering relative stabilities of chromium sulfides [34], CrS formation is the most likely possible in our case. Thus, it is fully consistent with our STEM-EDS data (Fig.9) but EDS measurements are far from the expected concentrations and stoichiometry (only about 10 at% of Cr and 1 at.% of S maximum). In addition to chromium sulfides, other chromium-rich products could also be present: metallic chromium,  $\text{Cr}_2\text{O}_3$ , nitrides or carbides. Unfortunately, phase identification using electron diffraction did not allow the identification of all phases located in the complex oxide layers.

The inhomogeneous alumina layers formed are less protective and could explain the formation of protuberated oxides and internal aluminum oxidation in the samples Al-48 and Al-82. A schematic illustration of oxide scales and their respective protectiveness formed with high sulfur content under steam conditions and low sulfur content under dry air are shown on figure 10.

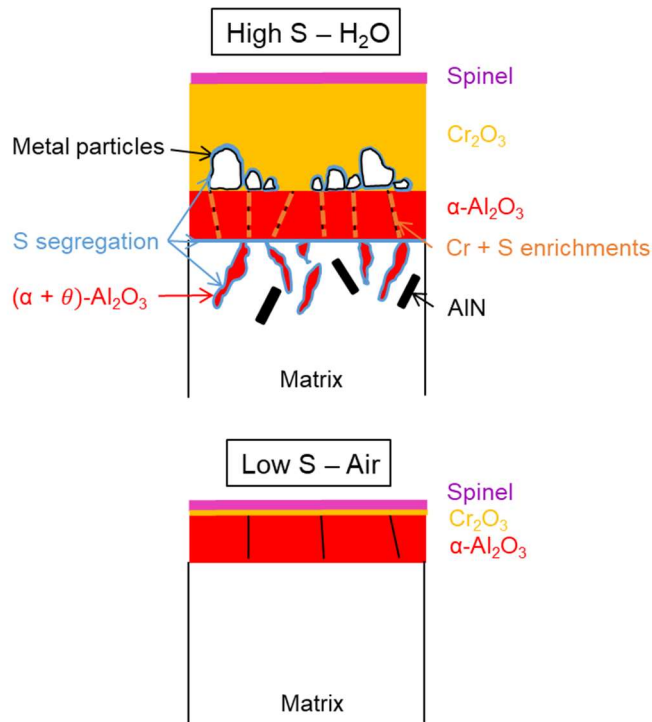


**Fig. 10** Schemes of oxide scales formed after oxidation under steam conditions of a high sulfur content alloy and after oxidation under dry air of a low sulfur content alloy

Furthermore, oxidation products formed are not the only problem in this application. Indeed metal particles were found in thick chromia layers when sulfur content isn't negligible (Figs.7.a, 9a). They might be the result of a fast initial chromium oxidation along matrix grain boundaries before the formation of the alumina layer. The number density of such metal particles is enhanced under steam conditions and could act as catalyst [61, 62] and promote coke formation during vapocracking applications. Since coke layers gradually cover surfaces and block pipes, decocking operation [63, 64] must be carried out which is deleterious for material integrity.

## CONCLUSIONS

- Higher sulfur contents lead to faster oxidation kinetics at 900°C under dry air. At sulfur concentrations above 40 ppm, the oxidation kinetic is significantly accelerated under water vapor conditions. A thin  $\alpha$  alumina layer always covers the alloy but it is protective against oxidation only at lower sulfur concentrations. Then, it is concluded that a sulfur content below about 30 ppm in wt% is necessary to achieve a protective alumina layer.
- Sulfur was detected along alumina interfaces, and inside the thin and continuous  $\alpha$  alumina layer where it is correlated with local chromium enrichments. The exact structure of these Cr and S rich features could not be identified (metal particles, oxides, sulfides, carbides) but these inhomogeneities clearly act as short-circuits diffusion through the alumina layer and affect its permeability.
- The thickness of the thin and continuous  $\alpha$  alumina layer is relatively similar under water vapor and air conditions, but alumina grains exhibit significantly smaller lateral dimensions when they grow under water vapor.

- [1] Da Silveira TL, May IL. Reformer furnaces: Materials, damage mechanisms and assessment. *Arabian Journal for Science and Engineering*. 2006;99-119.
- [2] Abe F, Kern TU, Viswanathan R, *Creep-Resistant Steels*. Elsevier; 2008.
- [3] De Almeida LH, Ribeiro AF, Le May I. Microstructural characterization of modified 25Cr–35Ni centrifugally cast steel furnace tubes. *Mater. Charact.* 2002;49:219-229.
- [4] Bonaccorsi L, Guglielmino E, Pino R, Servetto C, Sili A. Damage analysis in Fe–Cr–Ni centrifugally cast alloy tubes for reforming furnaces. *Eng. Fail. Anal.* 2014;36:65-74.
- [5] Young DJ. *HIGH TEMPERATURE OXIDATION AND CORROSION OF METALS*. Cambridge: ELSEVIER CORROSION SERIES; 2008.
- [6] Cottis B, Graham M, Lindsay R et al. *SHREIR'S CORROSION Volume I : Basic Concepts, High Temperature Corrosion*. The Netherlands : ELSEVIER-ACADEMIC PRESS; 1963.
- [7] Gao W, Li Z. *Developments in high-temperature corrosion and protection of materials*. Cambridge : WOODHEAD PUBLISHING IN MATERIALS; 2008.
- [8] Pons F, Thuillier J. Nickel- and chromium-base alloys possessing very-high resistance to carburization at very-high temperature. *US4248629A*. 1981.
- [9] Symoens SH, Olahova N, Munoz Gandarilla A et al. State-of-the-art of Coke Formation during Steam Cracking: Anti-Coking Surface Technologies. *Ind. Eng. Chem. Res.* 2018;57:16117-16136.
- [10] Facco A, Couvrat M, Magné D, Roussel M, Guillet A, Pareige C. Microstructure influence on creep properties of heat-resistant austenitic alloys with high aluminum content. *Mater. Sci. Eng. A*. 2020;139276.
- [11] Smith MA, Frazier WE, Pregger BA. Effect of sulfur on the cyclic oxidation behavior of a single crystalline, nickel-base superalloy. *Mater. Sci. Eng. A*. 1995;203:388-398.

- [12] Stringer J. The reactive element effect in high-temperature corrosion. *Mater. Sci. Eng. A*. 1989;120-121:129-137.
- [13] Smeggil JG, Funkenbusch AW, Bornstein NS. A relationship between indigenous impurity elements and protective oxide scale adherence characteristics. *Metall. Trans. A*. 1986;17:923-932.
- [14] Smialek JL, Morscher GN. Delayed alumina scale spallation on Rene'N5+Y: moisture effects and acoustic emission. *Mater. Sci. Eng. A*. 2002;332:11-24.
- [15] Stasik MC, Pettit FS, Meier GH, Ashary A, Smialek JL. Effects of reactive element additions and sulfur removal on the oxidation behavior of ferral alloys. *Scr. Metall. Mater.* 1994;31:1645-1650.
- [16] Delaunay D, Huntz AM, Lacombe P. Impurities influence on oxidation kinetics of Fe-Ni-Cr-Al alloys. *Corros. Sci.* 1984;24:13-25.
- [17] Abderrazik GB, Moulin G, Huntz AM, Berneron R. Influence of impurities, such as carbon and sulphur, on the high temperature oxidation behaviour of Fe<sub>72</sub>Cr<sub>23</sub>Al<sub>5</sub> alloys. *J. Mater. Sci.* 1984;19:3173-3184.
- [18] Wiemer D, Grabke HJ, Viefhaus H. Investigation on the influence of sulfur segregation on the adherence of protective oxide layers on high temperature materials. *Fresenius J. Anal. Chem.* 1991;341:402-405.
- [19] Lees DG. On the reasons for the effects of dispersions of stable oxides and additions of reactive elements on the adhesion and growth-mechanisms of chromia and alumina scales-the "sulfur effect". *Oxid. Met.* 1987;27:75-81.
- [20] Bonnell DA, Kiely J. Plasticity at Multiple Length Scales in Metal–Ceramic Interface Fracture. *Phys. Status Solidi A*. 1998;166:7-17.
- [21] Fox P, Lees DG, Lorimer GW. Sulfur segregation during the high-temperature oxidation of chromium. *Oxid. Met.* 1991;36:491-491.

- [22] Meier GH, Pettit FS, Smialek JL. The effects of reactive element additions and sulfur removal on the adherence of alumina to Ni- and Fe-base alloys. *Mater. Corros.* 1995;46:232-240.
- [23] Prescott R, Graham MJ. The formation of aluminum oxide scales on high-temperature alloys. *Oxid. Met.* 1992;38:233-254.
- [24] Lipkin DM, Clarke DR, Evans AG. Effect of interfacial carbon on adhesion and toughness of gold–sapphire interfaces. *Acta Mater.* 1998;46:4835-4850.
- [25] Kiely JD, Bonnell DA. Metal ceramic interface toughness I: Plasticity on multiple length scales. *J. Mater. Res.* 1998;13:2871-2880.
- [26] Pint BA. On the formation of interfacial and internal voids in  $\alpha$ -Al<sub>2</sub>O<sub>3</sub> scales. *Oxid. Met.* 1997;48:303-328.
- [27] Hance KO. EFFECTS OF WATER VAPOR ON THE OXIDATION BEHAVIOR OF ALUMINA AND CHROMIA FORMING SUPERALLOYS AT TEMPERATURES BETWEEN 700C AND 1000C. 2005. Available at: <http://d-scholarship.pitt.edu/6808>. Accessed February 19, 2018.
- [28] Saunders SRJ, Monteiro M, Rizzo F. The oxidation behaviour of metals and alloys at high temperatures in atmospheres containing water vapour: A review. *Prog. Mater. Sci.* 2008;53:775-837.
- [29] Janakiraman R, Meier GH, Pettit FS. The effect of water vapor on the oxidation of alloys that develop alumina scales for protection. *Metall. Mater. Trans. A.* 1999;30:2905-2913.
- [30] Maris-Sida MC, Meier GH, Pettit FS. Some water vapor effects during the oxidation of alloys that are  $\alpha$ -Al<sub>2</sub>O<sub>3</sub>- formers. *Metall. Mater. Trans. A.* 2003;34:2609-2619.
- [31] Maris-Sida MC. EFFECTS OF WATER VAPOR ON THE HIGH TEMPERATURE OXIDATION OF ALUMINA-FORMING COATINGS AND NI BASE SUPERALLOYS. 2005. Available at: <http://d-scholarship.pitt.edu/9454>. Accessed February 19, 2018.

- [32] Onal K, Maris-Sida MC, Meier GH, Pettit FS. Water vapor effects on the cyclic oxidation resistance of alumina forming alloys. *Mater. High Temp.* 2003;20:327-337.
- [33] Quadackers WJ, Wasserfuhr C, Khanna AS, Nickel H. Influence of sulphur impurity on oxidation behaviour of Ni–10Cr–9Al in air at 1000°C. *Mater. Sci. Technol.* 1988;4:1119-1125.
- [34] Huang TT, Richter R, Chang YL, Pfender E. Formation of aluminum oxide scales in sulfur-containing high temperature environments. *Metall. Trans. A.* 1985;16:2051-2059.
- [35] Aranda L, Schweitzer T, Mouton L et al. Kinetic and metallographic study of oxidation at high temperature of cast Ni 25Cr alloy in water vapour rich air. *Mater. High Temp.* 2015;32:530-538.
- [36] Götlind H, Liu F, Svensson JE, Halvarsson M, Johansson LG. The Effect of Water Vapor on the Initial Stages of Oxidation of the FeCrAl Alloy Kanthal AF at 900 °C. *Oxid. Met.* 2007;67:251-266.
- [37] Buscail H, Heinze S, Dufour P, Larpin JP. Water-vapor-effect on the oxidation of Fe-21.5 wt.%Cr-5.6 wt.%Al at 1000°C. *Oxid. Met.* 1997;47:445-464.
- [38] Brady MP, Yamamoto Y, Santella ML, Walker LR. Composition, Microstructure, and Water Vapor Effects on Internal/External Oxidation of Alumina-Forming Austenitic Stainless Steels. *Oxid. Met.* 2009;72:311-333.
- [39] Tancret F, Laigo J, Christien F, Gall RL, Furtado J. Phase transformations in Fe–Ni–Cr heat-resistant alloys for reformer tube applications. *Mater. Sci. Technol.* 2018;34:1333-1343.
- [40] De Almeida Soares GD, De Almeida LH, Da Silveira TL, Le May I. Niobium additions in HP heat-resistant cast stainless steels. *Materials Characterization.* 1992:387-396.
- [41] Shim SH, Duffy TS, Jeanloz R, Yoo CS, Iota V. Raman spectroscopy and x-ray diffraction of phase transitions in Cr<sub>2</sub>O<sub>3</sub> to 61 GPa. *Phys. Rev. B.* 2004;69:144107.

- [42] Hosterman B. Raman Spectroscopic Study of Solid Solution Spinel Oxides. UNLV Theses Diss. Prof. Pap. Capstones, 2011. Available at:  
<https://digitalscholarship.unlv.edu/thesesdissertations/1087>.
- [43] D'Ippolito V, Andreatti GB, Bersani D, Lottici PP. Raman fingerprint of chromate, aluminate and ferrite spinels. *Journal of Raman Spectroscopy*. 2015.
- [44] D. M. Lipkin and D. R. Clarke. Measurement of the stress in oxide scales formed by oxidation of alumina-forming alloys. *Oxid. Met.* 1996;45:267-280.
- [45] Boulloussa-Eiras S, Vanhaecke E, Zhao T, Chen D, Holmen A. Raman spectroscopy and X-ray diffraction study of the phase transformation of ZrO<sub>2</sub>-Al<sub>2</sub>O<sub>3</sub> and CeO<sub>2</sub>-Al<sub>2</sub>O<sub>3</sub> nanocomposites. *Catal. Today*. 2011;166:10-17.
- [46] Hakkar S, Achache S, Sanchette F, Mekhalif Z, Kamoun N, Boumaza A. Characterization by Photoluminescence and Raman Spectroscopy of the Oxide Scales Grown on the PM2000 at High Temperatures. *J. Mol. Eng. Mater.* 2019;7:1950003.
- [47] McNeil L, Grimsditch M, French RH. Vibrational Spectroscopy of Aluminum Nitride. *J Am Ceram Soc.* 1993;76:1132-1136.
- [48] Mercier-Bion F, Grousset S, Bouttemy M, Etcheberry A, Dillmann P, Neff D. Multi-technique investigation of sulfur phases in the corrosion product of iron corroded in long term anoxic conditions: from micrometric to nanometric scale. ECASIA 17, 2017. Available at: <https://hal-cea.archives-ouvertes.fr/cea-02331824>. Accessed March 24, 2020.
- [49] Gheno T, Monceau D, Oquab D, Cadoret Y. Characterization of sulfur distribution in Ni-based superalloy and thermal barrier coatings after high temperature oxidation : A SIMS analysis. *Oxid. Met.* 2010:95-113.
- [50] Gulbransen EA, Copan TP. Crystal Growths and the Corrosion of Iron. *Nature*. 1960;186:959-960.

- [51] Chevalier S. Diffusion of Oxygen in Thermally Grown Oxide Scales. *Defect and Diffusion Forum*, 2009. Available at: <https://www.scientific.net/DDF.289-292.405>. Accessed Apr. 25, 2019.
- [52] Clemens D, Bongartz K, Quadackers WJ, Nickel H, Holzbrecher H, Becker JS. Determination of lattice and grain boundary diffusion coefficients in protective alumina scales on high temperature alloys using SEM, TEM and SIMS. *Fresenius J. Anal. Chem.* 1995;353.
- [53] Balmain J, Huntz AM, Philibert J. *Defect Diffus. Forum.* 1997;143-147:1189.
- [54] Smialek JLG. Diffusion processes in Al<sub>2</sub>O<sub>3</sub> scales - Void growth, grain growth, and scale growth. High temperature corrosion, San Diego, 1981. Available at: <https://ntrs.nasa.gov/search.jsp?R=19830061020>. Accessed April 02, 2020.
- [55] Floreen S, Westbrook JH. Grain boundary segregation and the grain size dependence of strength of nickel-sulfur alloys. *Acta Metall.* 1969;17:1175-1181.
- [56] Tauber G, Grabke HJ. Grain Boundary Segregation of Sulfur, Nitrogen, and Carbon in  $\alpha$ -Iron. *Berichte Bunsenges. Für Phys. Chem.* 1978;82:298-302.
- [57] Ainslie NG, Hoffman RE, Seybolt AU. Sulfur segregation at  $\alpha$ -iron grain boundaries—I. *Acta Metall.* 1960;8:523-527.
- [58] Hou PY. Compositions at Al<sub>2</sub>O<sub>3</sub>/FeCrAl interfaces after high temperature oxidation. *Mater. Corros.* 2000;51:329-337.
- [59] Hou PY. Impurity Effects on Alumina Scale Growth. *J. Am. Ceram. Soc.* 2003;86:660-668.
- [60] Hou PY, Ackerman GD. Chemical state of segregants at Al<sub>2</sub>O<sub>3</sub>/alloy interfaces studied using Mxps. *Appl. Surf. Sci.* 2001;178:156-164.
- [61] Snoeck JW, Froment GF, Fowles M. Filamentous Carbon Formation and Gasification: Thermodynamics, Driving Force, Nucleation, and Steady-State Growth. *J. Catal.* 1997;169:240-249.

- [62] Baker RTK, Yates DJC, Dumesic JA. Filamentous Carbon Formation over Iron Surfaces. *Coke Formation on Metal Surfaces*. 1983;202:1-21.
- [63] Nishiyama Y, Anraku T, Sawaragi Y, Ogawa K, Okada H. Heat resistant nickel base alloy. *US6458318B1*, 2002.
- [64] Zimmermann G, Zychlinski W, Woerde HM, van den Oosterkamp P. Absolute Rates of Coke Formation: A Relative Measure for the Assessment of the Chemical Behavior of High-Temperature Steels of Different Sources. *Ind. Eng. Chem. Res.* 1998;37:4302-4305.